



Estimating model evidence using ensemble-based data assimilation with localization - The model selection problem

S. Metref^{*a}, A. Hannart^a, J. Ruiz^{a,b}, M. Bocquet^c, A. Carrassi^d and M. Ghil^{e,f}

^aIFAECI, CNRS-CONICET-UBA, Buenos Aires, Argentina.

^bCIMA-CONICET-University of Buenos Aires.

^cCEREA, joint laboratory École des Ponts ParisTech and EDF R&D, Université Paris-Est, Champs-sur-Marne, France.

^dNansen Environmental and Remote Sensing Center, Bergen, Norway.

^eGeosciences Department and Laboratoire de Météorologie Dynamique (CNRS and IPSL),
École Normale Supérieure and PSL Research University, Paris, France.

^fDept. of Atmospheric and Oceanic Sciences, University of California, Los Angeles, USA.

*Correspondence to: Sammy Metref, IFAECI, CNRS-CONICET-UBA, Pab. II, piso 2, Ciudad Universitaria 1428 Buenos Aires, Argentina, Tel.: +5411-4787-2693, Fax: +5411-4788-3572, e-mail: sammy.metref@cima.fcen.uba.ar

In recent years, there has been a growing interest in applying data assimilation (DA) methods, originally designed for state estimation, to the model selection problem. Along these lines, Carrassi et al. (2017) introduced the contextual formulation of model evidence (CME) and showed that CME can be efficiently computed using a hierarchy of ensemble-based DA procedures. Although Carrassi et al. (2017) analyzed the DA methods most commonly used for operational atmospheric and oceanic prediction worldwide, they did not study these methods in conjunction with localization to a specific domain. Yet any application of ensemble DA methods to realistic geophysical models requires the study of such localization. The present study extends the theory for estimating CME to ensemble DA methods with domain localization. The domain-localized CME (DL-CME) developed herein is tested for model selection with two models: (i) the Lorenz 40-variable mid-latitude atmospheric dynamics model (L95); and (ii) the simplified global atmospheric SPEEDY model. The CME is compared to the root-mean-square-error (RMSE) as a metric for model selection. The experiments show that CME improves systematically over the RMSE, and that such an improved skill is further enhanced by applying localization in the estimate of the CME, using the DL-CME. The potential use and range of applications of the CME and DL-CME as a model selection metric are also discussed.

1. Introduction and motivations

Model selection (Baum et al. 1970) is the problem of defining and using metrics to compare different models, or different versions of the same model that may differ by the model's parameters, its settings or its boundary conditions. Model selection, though, has received little attention from the geoscientific community, as compared to data assimilation (DA), which is by now a well-established field in the geosciences (Daley 1991; Ghil and Malanotte-Rizzoli 1991; Bennett 1992; Kalnay 2003; Asch et al. 2016), and which has focused so far mainly on estimating high-dimensional states of the atmosphere (Whitaker et al. 2008; Buehner et al. 2010), of the ocean (Lermusiaux 2006; Sakov et al. 2012) and of the climate system as a whole (Saha et al. 2010; Saha et al. 2014). Even nowadays, a common practice to evaluate models at operational centers is to compare visually model outputs to observations or, more quantitatively, to compute the model-to-data root-mean-square error (RMSE).

Some attempts to analytically address the model selection problem have been successful (e.g., Winiarek et al. 2011) but only under specific assumptions that may not be realistic for large-dimensional geoscientific applications. Numerical methodologies that may be computationally affordable for high-dimensional problems have also been proposed in recent years (Elsheikh et al. 2014a,b; Otsuka and Miyoshi 2015; Reich and Cotter 2015; Carson et al. 2017; Carrassi et al. 2017). Several of these approaches advocate the use of the marginal likelihood of the data — also called model evidence — for model selection. Along these lines, the contextual formulation of model evidence (CME), first proposed by Hannart et al. (2016b) and fleshed out by Carrassi et al. (2017), exploits DA techniques to approach the model selection problem.

Carrassi et al. (2017) provide the analytic formulae to compute the CME using several state-of-the-art Gaussian ensemble DA methods and demonstrate the benefits of CME as a model selecting tool. Their study thus started to answer the first theoretical and practical research questions that had to be addressed to make the CME suitable for model selection operationally in weather forecasting centers.

Nevertheless, a number of issues still remain to be tackled in order to proceed to the operational implementation of the CME. Among these, one key issue is the use of spatial localization — called henceforth simply localization — in ensemble-based DA. Indeed, when applied to large-dimensional models, the ensemble based DA methods of Carrassi et al. (2017) to compute CME would fail unless localization is properly incorporated. Even though localization is a widely established practice in ensemble DA, and has also generated a substantial literature (e.g., Houtekamer and Mitchell 2001; Hamill et al. 2001; Ott et al. 2004 and Sakov and Bertino 2011), it is still matter of intense research.

Localization originally arisen as a countermeasure to the sampling issue due to our attempt to describe uncertainty in high-dimension using a very limited ensemble. Help in overcoming this problem comes from the fact that many physical systems, and notably the atmosphere and ocean, tend to have small long-distance correlations, i.e., the actual error covariances are sparse (e.g., Ghil et al. 1979; Balgovind et al. 1983). For such systems, localization can — without degrading too severely the physical systems' representation — set long-distance correlations to zero and only model the close-to-diagonal terms in the covariance matrix.

Many localization techniques exist to achieve sufficiently accurate approximations of the covariance matrix along these lines. These techniques, though, do lead to a change in the structure of the matrices manipulated during the DA process. Hence, in the CME context, the challenge is to adapt its original formulation to the need for localization in the underlying DA process. This study aims, therefore, to extend CME theory, as presented in Carrassi et al. (2017), to include localization and to apply it to a quasi-realistic atmospheric model of intermediate complexity.

The structure of the paper is as follow. Section 2 recalls the benefits of approaching model evidence using the DA framework. A more extensive discussion of these benefits can be found in Hannart et al. (2016b). Section 3 first introduces the notion of localization in general, and the domain localization technique in particular. The application of domain localization in the CME computation is hereafter referred to as the domain-localized

CME (DL-CME), and it is also presented in Section 3. Section 4 implements the two CME formulations (with and without localization) and compares them to the RMSE as model selection indicators with the RMSE in various numerical experiments based on the 40-dimensional Lorenz-95 model. Section 5 applies these indicators to a parameter selection problem using the simplified global atmospheric model called SPEEDY (Molteni 2003; Kucharski 2006). Section 6 finally provides a summary, conclusions and future directions.

2. Model evidence and data assimilation

Let us assume that a model \mathcal{M} describes an unknown process at time k , as a M -dimensional state \mathbf{x}_k , that we only perceive via a set of partial, d -dimensional observations \mathbf{y}_k .

The model \mathcal{M} . The model \mathcal{M} simulates the unknown process

$$\mathbf{x}_k = \mathcal{M}_{k:k-1}(\mathbf{x}_{k-1}) + \boldsymbol{\eta}_k, \quad (1)$$

where $\mathcal{M}_{k:k-1} : \mathbb{R}^M \rightarrow \mathbb{R}^M$ propagates the state $\mathbf{x} \in \mathbb{R}^M$ from time t_{k-1} to time t_k . The dimension M of the model state can be decomposed as $M = \text{Card}(\Lambda) \times \text{Card}(\Gamma)$, where Λ is the space of the physical variables and Γ is the spatial resolution of the model.

In general, $\boldsymbol{\eta}_k \in \mathbb{R}^M$ is the model error — represented most often by an additive stochastic white noise — but here we shall assume that the model is perfect, i.e., $\boldsymbol{\eta}_k \equiv 0$. The implications of this assumption on the computation of the CME are substantial, cf. Carrassi et al. (2017), but we have reason to believe that it does not affect very much our conclusions about the impact of localization on the CME and its comparison with the RMSE. This perfect model assumption will be removed in subsequent studies.

The set of observations \mathbf{y} . The observation vector $\mathbf{y}_k \in \mathbb{R}^d$ is related to the state vector \mathbf{x}_k according to the observation model

$$\mathbf{y}_k = \mathcal{H}_k(\mathbf{x}_k) + \boldsymbol{\epsilon}_k. \quad (2)$$

Here $\mathcal{H}_k : \mathbb{R}^M \rightarrow \mathbb{R}^d$ is the observational operator at time k and $\boldsymbol{\epsilon}_k$ is the observation error, represented here as an additive

stochastic white noise with zero mean and covariance \mathbf{R} , which is assumed to be constant in time.

Having introduced the observational model, \mathcal{H} , in Eq. 2, we can now define its liberation around \mathbf{x}_k , to be used in the DA process (cf. section 2.2), as the $d \times M$ matrix \mathbf{H}_k , and the associated transpose \mathbf{H}^T .

2.1. CME for model selection

Using a model of type \mathcal{M} and the set of observations $\mathbf{y}_{k:1} = \{\mathbf{y}_k, \mathbf{y}_{k-1}, \dots, \mathbf{y}_2, \mathbf{y}_1\}$, the goal of model selection is to define a metric based on them, and apply it to identify the best model. Several metrics for model selection are defined in the literature (Akaike 1974; Schwarz 1978; Burnham and Anderson 2002). In the present article, we focus on model evidence as the metric of choice (Elsheikh et al. 2014a,b; Otsuka and Miyoshi 2015; Reich and Cotter 2015; Carson et al. 2017; Carrassi et al. 2017).

2.1.1. Model evidence

Let us define the ideal infinite set of observations as $\mathbf{y}_{k:} = \{\mathbf{y}_k, \mathbf{y}_{k-1}, \dots, \mathbf{y}_1, \mathbf{y}_0, \dots, \mathbf{y}_{-\infty}\}$. The marginal likelihood of $\mathbf{y}_{k:}$, given \mathcal{M} , is calculated as

$$p(\mathbf{y}_{k:}|\mathcal{M}) = \int d\mathbf{x} p(\mathbf{y}_{k:}|\mathbf{x}, \mathcal{M})p(\mathbf{x}). \quad (3)$$

This likelihood is also referred to as model evidence.

Note that, in the context of model evaluation, one should rather be interested in estimating the probability of the model conditioned to the observations $p(\mathcal{M}|\mathbf{y}_{k:})$. Yet, model evidence can be used to construct a metric for model selection or model comparison between two models \mathcal{M}_0 and \mathcal{M}_1 . To see this, let us write the ratio of the two posterior distributions, each one relative to models \mathcal{M}_0 and \mathcal{M}_1 respectively, conditioned on the same set of observations

$$\frac{p(\mathcal{M}_1|\mathbf{y}_{k:})}{p(\mathcal{M}_0|\mathbf{y}_{k:})} = \frac{p(\mathbf{y}_{k:}|\mathcal{M}_1) p(\mathcal{M}_1)}{p(\mathbf{y}_{k:}|\mathcal{M}_0) p(\mathcal{M}_0)} \quad (4)$$

Equation (4) computes the ratio of the posterior model probability density functions (pdfs) and we see that it is proportional to the ratio of the model evidences – the Bayesian factor – times the ratio of the prior model pdfs. The latter are

difficult to evaluate in practice, but, it is often legitimate to assume that the prior pdfs of the two models are the same, provided that we do not possess enough information to favor one model over the other. In this case, we see how the Bayesian factor provides an estimate of the model pdf ratio. In any case, the Bayesian factor is the scalar that updates the ratio of prior model pdfs to the ratio of posterior model pdfs.

In this sense, the ratio of the two model evidences $p(\mathbf{y}_{k:}|\mathcal{M}_1)/p(\mathbf{y}_{k:}|\mathcal{M}_0)$ can be considered as a selection indicator that favors one model or the other, depending on $p(\mathbf{y}_{k:}|\mathcal{M}_1)/p(\mathbf{y}_{k:}|\mathcal{M}_0) \leq 1$. More conveniently, one can look at the difference between their respective logarithms, and write the model selection indicator as

$$\Delta_{\mathbf{y}_{k:}}(\mathcal{M}_0, \mathcal{M}_1) = \ln\{p(\mathbf{y}_{k:}|\mathcal{M}_1)\} - \ln\{p(\mathbf{y}_{k:}|\mathcal{M}_0)\}. \quad (5)$$

We use the indicator $\Delta_{\mathbf{y}_{k:}}(\mathcal{M}_0, \mathcal{M}_1)$ in the following experiments, and the model selection criterion becomes $\Delta_{\mathbf{y}_{k:}}(\mathcal{M}_0, \mathcal{M}_1) \leq 0$.

Previously, model evidence calculations were mainly based on Monte-Carlo methods, as in [Elsheikh et al. \(2014a\)](#), [Elsheikh et al. \(2014b\)](#) and [Carson et al. \(2017\)](#). In the present article, we focus on the use of DA for this purpose, following and expanding the work in [Carrassi et al. \(2017\)](#).

2.1.2. Contextual model evidence

If the model is autonomous, one can condition model evidence to the initial observation \mathbf{y}_0 of the set, and write

$$p(\mathbf{y}_{k:}|\mathcal{M}) = p(\mathbf{y}_{k:1}|\mathbf{y}_0)p(\mathbf{y}_0) \quad (6)$$

where the explicit dependence on \mathcal{M} has been dropped on the right-hand side, for the sake of clarity.

An alternative formulation of the model evidence, with also a potential computational gain, is to no longer try to estimate the climatological model evidence $p(\mathbf{y}_{k:}|\mathcal{M})$ – which is difficult to estimate accurately and which does not inform on the present context of the system – the so called contextual model evidence (CME), $p(\mathbf{y}_{k:1}|\mathbf{y}_0)$ ([Carrassi et al. 2017](#)). This new contextual

view of model evidence implicitly assumes that all information from past observations is conveyed by conditioning on \mathbf{y}_0 .

Marginalizing over \mathbf{x}_0 yields

$$p(\mathbf{y}_{k:1}|\mathbf{y}_0) = \int d\mathbf{x}_0 p(\mathbf{y}_{k:1}|\mathbf{x}_0)p(\mathbf{x}_0|\mathbf{y}_0) \quad (7)$$

Therefore, the two terms needed to compute the CME are:

- the conditional pdf, $p(\mathbf{x}_0|\mathbf{y}_0)$, and
- the likelihood of the observations, $p(\mathbf{y}_{k:1}|\mathbf{x}_0)$.

The conditional pdf $p(\mathbf{x}_0|\mathbf{y}_0)$ is the posterior pdf, or analysis, produced by the state estimation DA process. The observational likelihood $p(\mathbf{y}_{k:1}|\mathbf{x}_0)$ is often a given quantity (or at least considered as such) of the state estimation DA problem. Hence, as shown in [Carrassi et al. \(2017\)](#), the CME can be obtained as a by-product of a DA algorithm designed to assimilate the data \mathbf{y} into the model \mathcal{M} .

2.2. The CME's EnKF-formulation

We present here the CME formulation based on the ensemble Kalman filter (EnKF, [Evensen 2009](#)). The choice of the EnKF among other, possibly even more accurate, methods to compute CME, is motivated by its great ratio cost/benefit. It was shown in [Carrassi et al. \(2017\)](#), that it achieves very high skill in evaluating the CME, only slightly lower than other more sophisticated methods, but at a much lower computational cost.

The EnKF-formulation of the CME comes as a by-product of the EnKF DA process that gives an approximation of model evidence $p(\mathbf{y}_{K:1}|\mathbf{y}_0)$. Over the evidencing window $K = t_k - t_0$, the CME is calculated as

$$p(\mathbf{y}_{K:1}|\mathbf{y}_0) \approx \prod_{k=0}^K (2\pi)^{-\frac{d}{2}} |\Sigma_k|^{-\frac{1}{2}} \times \exp \left\{ -\frac{1}{2} [\mathbf{y}_k - \mathcal{H}_k(\mathbf{x}_k^f)]^T \Sigma_k^{-1} [\mathbf{y}_k - \mathcal{H}_k(\mathbf{x}_k^f)] \right\}, \quad (8)$$

with $\Sigma_k = \mathbf{H}_k \mathbf{P}_k^f \mathbf{H}_k^T + \mathbf{R}$, where \mathbf{P}_k^f is the prior error covariance matrix at time k .

Two different proofs of the EnKF-based CME, Eq. 8, are proposed using a stochastic version of the EnKF in [Hannart et al. \(2016b\)](#) and a deterministic one in [Carrassi et al. \(2017\)](#), and are both referred to as the global CME (G-CME) hereafter.

An efficient alternative to compute the G-CME is presented in [Appendix A](#) and is used throughout the present article. This implementation stands on the assumption that \mathbf{R} is diagonal, i.e., that the observations are mutually uncorrelated, an assumption, nonetheless, often made in the geosciences. A significant improvement in this alternative G-CME implementation is its reducing the computational cost from depending on the size of the state vector M to depending on the ensemble size N , which is generally much lower, $N \ll M$.

3. CME and domain localization

This section presents a new formulation of the CME that takes into account domain localization. We describe first, in [section 3.1](#), how domain localization is implemented within the DA process, and then the domain-localized CME (DL-CME) in [section 3.2](#).

3.1. Domain localization

3.1.1. The basic idea

Domain localization consists in updating separately, at each spatial gridpoint $s \in \Gamma$, all the physical variables $\{\mathbf{x}_{s,l}\}$, with $l \in \Lambda$, by assimilating only neighboring observations. This idea goes back to earlier forms of DA, like the successive correction method ([Cressman 1959](#); [Ghil et al. 1979](#); [Ghil and Malanotte-Rizzoli 1991](#)). We describe here the implementation known as local analysis ([Houtekamer and Mitchell 2001](#); [Ott et al. 2002, 2004](#); [Hunt et al. 2007](#)).

The first step of local analysis consists in selecting the observations within a disk centered on the spatial gridpoint $s \in \Gamma$ we wish to update; the radius of this disk is a predefined parameter ρ_{cut} , called the cut-off radius. This type of selection process is often called the box-car scheme, as opposed to schemes that gradually taper off the weights given to observations, from 1 to 0. Note that in general the cut-off radius depends on the physical variable to be analyzed.

We call the resulting reduced observation vector $\mathbf{y}_{|s}$, and its size \tilde{d} . It is then also necessary to restrict the observation error covariance matrix \mathbf{R} to a local, and hence of smaller dimension, matrix $\mathbf{R}_{|s}$. The resulting analysis after the first step alone may, however, present abrupt discontinuities when crossing the

boundary of the observation disk and have, therefore, a deleterious side-effect, whose elimination or mitigation requires a second analysis step.

The second step in local analysis applies a localization function to the inverse matrix $\mathbf{R}_{|s}^{-1}$, called precision matrix, and it produces a smoother global update. The localization function is in fact the Schur product ([Hunt et al. 2007](#)) of $\mathbf{R}_{|s}^{-1}$ by the diagonal localization matrix \mathbf{L} giving

$$\tilde{\mathbf{R}}_{|s}^{-1} = \mathbf{L} \circ \mathbf{R}_{|s}^{-1} = (\mathbf{R}_{|s}^{-1})_{i,j} \cdot (\mathbf{L})_{i,j} \quad (9)$$

where $(\mathbf{L})_{i,i}$ is equal to 1 if $i = s$ and it decreases gradually to 0 outside of the disk of radius ρ_{loc} , called the localization radius, where $\rho_{\text{loc}} \geq \rho_{\text{cut}}$. Hence, the further an observation lies from s , the more its observation error variance is increased and its impact on the local analysis is decreased.

3.1.2. The LETKF

The ensemble transform Kalman filter (ETKF; [Bishop et al. 2001](#)) is a deterministic EnKF performing the analysis in the ensemble space. The ETKF computes the updated ensemble $\mathbf{E}^a = [\mathbf{x}_1^a, \dots, \mathbf{x}_N^a] \in \mathbb{R}^{M \times N}$, with \mathbf{x}_i^a the N ensemble members, such that

$$\mathbf{E}^a = \bar{\mathbf{x}}^f \mathbf{1}^T + \mathbf{X}^f \left(\mathbf{w}^a \mathbf{1}^T + \sqrt{N-1} \tilde{\mathbf{P}}^a \right). \quad (10)$$

Here $\tilde{\mathbf{P}}^a = \{(\mathbf{H}\mathbf{X}^f)^T \mathbf{R}^{-1} (\mathbf{H}\mathbf{X}^f) + (N-1)\mathbf{I}_N\}^{-1}$ and $\mathbf{w}^a = \tilde{\mathbf{P}}^a (\mathbf{H}\mathbf{X}^f)^T \mathbf{R}^{-1} (\mathbf{y} - \mathcal{H}_k(\bar{\mathbf{x}}^f))$, and the analysis ensemble \mathbf{E}^a is given by a linear combination of the forecast ensemble mean $\bar{\mathbf{x}}^f \in \mathbb{R}^M$ and the forecast ensemble anomalies in \mathbf{X}^f . Finally, $\mathbf{1}^T = [1, \dots, 1] \in \mathbb{R}^M$ and \mathbf{I}_N is the $N \times N$ identity matrix.

The domain localization applied to the ETKF gives the local ensemble transform Kalman filter (LETKF, [Hunt et al. 2007](#)). In the LETKF, a separate analysis is performed for each model gridpoint $s \in \Gamma$ of the spatial grid and the resulting update affects each physical variable $l \in \Lambda$ at s . The DA is performed using localized observations, i.e., the observation precision matrix is $\tilde{\mathbf{R}}_{|s}^{-1}$.

3.2. Domain-localized CME

In order to formulate the CME with domain localization, we start with the general case of an observation subvector of generic

nature. In section 3.2.1, the case of the trivial evidencing window $K = 1$ is treated first. Second, we address the inconsistency that arises when $K \geq 2$ and show how to remove it by using realistic approximations. In section 3.2.2, we derive from the general case a formulation of the local CME. Finally, in section 3.2.3, we propose a heuristic global model selection indicator based on local CMEs, the DL-CME.

3.2.1. CME of an observation subvector

Let us consider first the problem of estimating the CME of $\hat{\mathbf{y}}_{K:1}$, a subvector of the original observation vector $\mathbf{y}_{K:1}$. Such a subvector may be obtained either by selecting a subset of observation types or by a spatial localization or both. The corresponding CME is just a particular case of the original DA, i.e., of the DA for the complete observation vector, as given by Eq. ((7)), and can be obtained from it. Indeed, if the evidencing window has length $K = 1$, the contextual evidence of $\hat{\mathbf{y}}_1$ becomes

$$p(\hat{\mathbf{y}}_1|\mathbf{y}_{0:}) = \int d\mathbf{x}_0 p(\hat{\mathbf{y}}_1|\mathbf{x}_0)p(\mathbf{x}_0|\mathbf{y}_{0:}). \quad (11)$$

Both pdfs in the integrand above are by-products of the original DA: $p(\mathbf{x}_0|\mathbf{y}_0)$ is the original posterior pdf at time t_0 and the sub-sampled likelihood $p(\hat{\mathbf{y}}_1|\mathbf{x}_0)$ also stems from the original DA process. Using the EnKF formalism, one can compute the CME for this subvector using Eq. (8) which in this case leads to

$$p(\hat{\mathbf{y}}_1|\mathbf{y}_{0:}) \approx (2\pi)^{-\frac{d}{2}} |\hat{\Sigma}_1|^{-\frac{1}{2}} \times \exp \left\{ -\frac{1}{2} [\hat{\mathbf{y}}_1 - \hat{\mathcal{H}}_1(\mathbf{x}_1^f)]^T \hat{\Sigma}_1^{-1} [\hat{\mathbf{y}}_1 - \hat{\mathcal{H}}_1(\mathbf{x}_1^f)] \right\}. \quad (12)$$

Here $\hat{\Sigma}_1 = \hat{\mathbf{H}}_1 \mathbf{P}_1^f \hat{\mathbf{H}}_1^T + \hat{\mathbf{R}}$, where $\hat{\mathcal{H}}_1$, $\hat{\mathbf{H}}_1$ and $\hat{\mathbf{R}}$ are the observation operator, its linearization and the observation error covariance matrix corresponding to the observation subvector, respectively. Note that $(\mathbf{x}_1^f, \mathbf{P}_1^f)$ are the forecast products of the original DA.

If the evidencing window is longer, $K > 1$, we decompose the contextual evidence — as shown in Carrassi et al. 2017 — as

$$\begin{aligned} p(\hat{\mathbf{y}}_{K:1}|\mathbf{y}_{0:}) &= p(\hat{\mathbf{y}}_1|\mathbf{y}_{0:}) \prod_{k=2}^K p(\hat{\mathbf{y}}_k|\hat{\mathbf{y}}_{k-1:0}, \mathbf{y}_{0:}) \\ &= \int d\mathbf{x}_1 p(\hat{\mathbf{y}}_1|\mathbf{x}_0)p(\mathbf{x}_0|\mathbf{y}_{0:}) \\ &\quad \times \prod_{k=2}^K \int d\mathbf{x}_k p(\hat{\mathbf{y}}_k|\mathbf{x}_{k-1})p(\mathbf{x}_{k-1}|\hat{\mathbf{y}}_{k-1}). \end{aligned} \quad (13)$$

The $p(\hat{\mathbf{y}}_1|\mathbf{y}_{0:})$ factor in Eq. (13) corresponds to the case $K = 1$ and it can be computed from the original DA process using Eq. (12). The sub-sampled likelihoods $p(\hat{\mathbf{y}}_k|\mathbf{x}_{k-1})$ are also easily computable since the likelihood of the observation is usually given in a state-estimation process.

The pdf of the system's state, conditional on the observation subvectors $p(\mathbf{x}_{k-1}|\hat{\mathbf{y}}_{k-1})$ for $2 \leq k \leq K$, however, requires a dedicated DA of the observation subvectors. It seems desirable to estimate these exact pdfs but the forecast-assimilation process required to do so may — depending on the nature of the observation subvectors — involve an insufficiently observed system and the DA algorithm may, therefore, fail to converge (cf. section 5.1.3).

In such a situation, approximating $p(\mathbf{x}_{k-1}|\hat{\mathbf{y}}_{k-1})$ by the original posterior pdf, $p(\mathbf{x}_{k-1}|\mathbf{y}_{k-1})$, is a possibility when the evidencing window K is short enough. In this case, the EnKF-formulation can be used to compute the CME as

$$\begin{aligned} p(\hat{\mathbf{y}}_{K:1}|\mathbf{y}_{0:}) &\simeq \prod_{k=0}^K (2\pi)^{-\frac{d}{2}} |\hat{\Sigma}_k|^{-\frac{1}{2}} \\ &\quad \times \exp \left\{ -\frac{1}{2} [\hat{\mathbf{y}}_k - \hat{\mathcal{H}}_k(\mathbf{x}_k^f)]^T \hat{\Sigma}_k^{-1} [\hat{\mathbf{y}}_k - \hat{\mathcal{H}}_k(\mathbf{x}_k^f)] \right\}, \end{aligned} \quad (14)$$

where $\hat{\Sigma}_k = \hat{\mathbf{H}}_k \mathbf{P}_k^f \hat{\mathbf{H}}_k^T + \hat{\mathbf{R}}$. Using instead of the above approximation the correct pdfs of the system's state, conditional on the observation subvector $p(\mathbf{x}_{k-1}|\hat{\mathbf{y}}_{k-1})$, would require computing the ad-hoc $\hat{\mathbf{P}}_k^f$ in $\hat{\Sigma}_k$, instead of \mathbf{P}_k^f .

3.2.2. Local CME

In the same spirit as the local analysis above, we want to locally compute the CME at each spatial gridpoint $s \in \Gamma$. The reduced observation vectors $\mathbf{y}_{k|s}$ can be considered as observation

subvectors $\hat{\mathbf{y}}_k$ and we can use, therewith, the formalism of section 3.2.1.

Hence, for each spatial gridpoint s , the local CME can be obtained from Eq. (14), yielding

$$p(\mathbf{y}_{K:1|s}|\mathbf{y}_{0:}) \approx \prod_{k=0}^K (2\pi)^{-\frac{d}{2}} |\tilde{\Sigma}_k|^{-\frac{1}{2}} \times \exp \left\{ -\frac{1}{2} (\mathbf{y}_{k|s} - \mathcal{H}_k(\mathbf{x}_k^f)_{|s})^T \tilde{\Sigma}_k^{-1} (\mathbf{y}_{k|s} - \mathcal{H}_k(\mathbf{x}_k^f)_{|s}) \right\}; \quad (15)$$

here $\tilde{\Sigma}_k = \mathbf{H}_{k|s} \mathbf{P}_k^f \mathbf{H}_{k|s}^T + \tilde{\mathbf{R}}_{|s}$; $\mathcal{H}_k(\cdot)_{|s}$ and $\mathbf{H}_{k|s}$ are, respectively, the restrictions of the nonlinear and the linearized observation operator to the neighborhood of s . In other words, at the spatial point s , the local CME returns the CME of the observations that have affected its analysis.

Remark that, in the case of domain localization, it is not necessary to approximate the conditional pdf of the system's state on the observation subvectors by the original posterior pdf, since $\mathbf{H}_{k|s} \mathbf{P}_k^f \mathbf{H}_{k|s}^T$ is already the local approximation of $\mathbf{H}_k \mathbf{P}_k^f \mathbf{H}_k^T$. Nonetheless, the $\mathbf{y}_{k|s}$ observation vectors represent a *tube* of observations spread in time over the evidencing window but confined to the same local domain. Due, however, to the physical evolution of the error covariances, such a static tube may not be as relevant for DA and evidencing as would be a dynamic tube that follows local domains that are covariant with the flow (Bocquet 2016). The implementation of such covariant localization techniques is not required, though, for the short evidencing windows used in the following, so that we apply Eq. (15) without such corrections.

3.2.3. The DL-CME

Creating a global indicator from local CMEs is not theoretically straightforward. We propose instead a global heuristic indicator for model selection $\tilde{p}(\mathbf{y}_{K:1}|\mathbf{y}_{0:})$, that we call the DL-CME,

$$\tilde{p}(\mathbf{y}_{K:1}|\mathbf{y}_{0:}) = \exp \left\{ \sum_{s \in \Gamma} w(s) \ln \{p(\mathbf{y}_{K:1|s}|\mathbf{y}_{0:})\} \right\}; \quad (16)$$

here $w(s)$ are positive, model grid-dependent coefficients, inversely proportional to the localization radius, that weight the logarithms of the local CMEs, such that $\sum_{s \in \Gamma} w(s) = 1$. For instance, in the L95 experiments of section 4, all the $w(s)$ weights are set to be equal since the localization radius is constant

throughout the domain. However, in the SPEEDY experiments (section 5), $w(s)$ vary with the latitude as the number of gridpoints per local domain does.

3.3. Brief review of covariance localization.

Another widely used localization technique is covariance localization, also called the Schur localization (Houtekamer and Mitchell 2001). This localization consists in restricting the spatial impact of the unrealistic correlations due to the subsampling of the ensemble-based covariances, by directly applying a smoothing function onto the forecast error covariance matrix.

This technique can be applied to the computation of the CME in the same vein as DL-CME above, in order to take into account the actual covariances used by the DA. Details of the derivation of the CME formulation using covariance localization are presented in Appendix B. The computational cost remains the same as for the original EnKF-formulation plus the significant cost of a $M \times M$ Schur product.

This alternative approach to CME localization can also be applied to large-dimensional systems, but only if combined with sophisticated numerical techniques to make it computationally feasible. For this reason, covariance localization will not be discussed furthermore in the present article. Further studies investigating this matter should follow.

4. Numerical experiments with a toy model

The numerical experiments are designed to: (i) study numerically the performance of the global and local CME as a model selection indicator and to compare it with the RMSE that is widely used for the same purposes; and (ii) analyze the impact of domain localization in the computation of the CME. These experiments use the Lorenz-95 (L95: Lorenz 1996; Lorenz and Emanuel 1998) model.

4.1. Experimental setup

4.1.1. The Lorenz-95 model

The one-dimensional L95 model is a minimal representation of atmospheric flow along a mid-latitude zonal circle with $M = 40$ variables $\{x_i : i = 1, \dots, 40\}$. In this case, $\text{Card}(\Gamma) =$

M and $\text{Card}(\Lambda) = 1$, i.e., one single physical variable, such as temperature or vorticity, is defined at each grid point.

The model equations, according to [Lorenz and Emanuel \(1998\)](#), are the following

$$\frac{dx_i}{dt} = (x_{i+1} - x_{i-2})x_{i-1} - x_i + F, \quad (17)$$

for $i = 1, \dots, M$ and F represents the external forcing. The model integration is performed using a fourth-order Runge-Kutta scheme with a time step $\delta t = 0.05$, in nondimensional units for which unity corresponds to 5 days ([Lorenz 1996](#)).

In our model selection problem, we consider the correct model given by Eq. (17) with $F = F_1 = 8$. This value leads to chaotic behavior of the model, with a doubling time of errors equal to 2.1 days ([Lorenz 1996](#)). We then generate various incorrect models, each of them with a different forcing term $F_0 \neq F_1$.

4.1.2. The DA implementation

Observations are generated by sampling the true trajectory \mathbf{x}^t , every DA interval $\Delta t = 0.05$, using Eq. (2) with $\epsilon \sim \mathcal{N}(0, 1)$ and $\mathbf{H}_k = \mathbf{I}_{40}$, so that the full system is observed. The correct observation error covariance, $\mathbf{R} = \mathbf{I}_{40}$, is used in the DA. The experiments are run over $T = 5 \times 10^4$ DA cycles, after a spin-up of $T_{\text{su}} = 10^4$ DA cycles.

The DA method used throughout the present section is the LETKF described in section 3.1.2. The localization matrix, \mathbf{L} , is diagonal with coefficients defined by $\left\{ G \left(|\tilde{d}/2 - i|/\rho_{\text{loc}} \right) \right\}_{i,i}$, where \tilde{d} is the size of the reduced observation error covariance matrix, ρ_{loc} is the localization radius and G is the Gaspari-Cohn function ([Gaspari and Cohn 1999](#)) displayed in Eq. (27) of [Appendix B](#).

The performance of the DA algorithm is evaluated using the RMSE of the analysis with respect to the truth

$$\text{RMSE}^t = \sqrt{\frac{1}{M} \sum_{i=1}^M (x_i^a - x_i^t)^2}, \quad (18)$$

with $\mathbf{x}^t = (x_i^t)_{i=1:M}$ and $\mathbf{x}^a = (x_i^a)_{i=1:M}$ being the true and estimated state. Here and elsewhere we follow the superscript notation $\{t, a, f, o\}$ proposed by [Ide et al. \(1997\)](#) for the truth,

the analysis (i.e. the estimated state), the forecast and the observations.

The accuracy of the model selection is assessed based on the RMSE of the forecast with respect to the observations

$$\text{RMSE} = \sqrt{\frac{1}{d} \sum_{i=1}^d (\mathcal{H}(x_i^f) - y_i)^2}. \quad (19)$$

Model evidence, for both the G-CME and the DL-CME formulations, is evaluated over the evidencing window $K = t_k - t_0$. Unless otherwise stated, we set here $K = 1$, which means that the model evidence is computed only for one DA cycle.

4.2. Numerical results

4.2.1. CME versus RMSE

In this subsection, we focus on the performance of the G-CME (Eq. 8) — i.e., without localization — as the model selection indicator, and compare it with that of the RMSE.

For each model configuration, i.e. for each choice of the forcing F , a DA is performed using the setup described in section 4.1.2, with a 40-member ensemble ($N = 40$), without localization and with a coefficient of inflation tuned to provide the smallest RMSE^t (Eq. 18) for each DA. At each cycle of the experiment, the G-CME and RMSE indicators are computed.

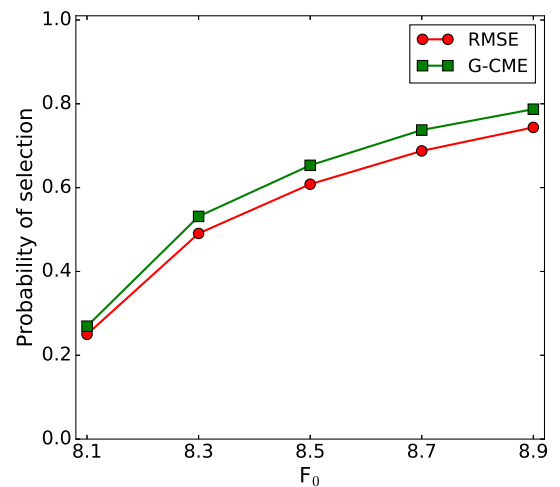


Figure 1. Probability of selecting the correct model, with $F_1 = 8$, vs. a particular incorrect model, with $F_0 = 8.1, 8.3, 8.5, 8.7$ and 8.9 . The probabilities are calculated using one of the two model selection indicators: RMSE (solid red line and circles) and G-CME (solid green line and squares), for a 40-member ensemble.

Probability of selection. We first look at the probability of selection of the correct model for each indicator; that is, $2R - 1$ where R is computed by counting how many times each indicator chooses the correct model over the incorrect one, out of the total of $T = 5 \times 10^4$ cycles. Thus, a random classifier will produce a probability of selection equal to 0 and a perfect classifier will produce one equal to 1. This allows us to evaluate the reliability of the indicators in terms of model selection. Then, by repeating the computation for different values of F_0 , we deduce the sensitivity of either indicator to the discrepancy $F_1 - F_0$ between correct and incorrect models.

The probabilities of selection are given in Figure 1. The incorrect models are simulated with the forcings $F_0 = 8.1, 8.3, 8.5, 8.7, 8.9$ plotted on the x -axis. Note that the larger the forcing F_0 , the easier it should be to select the correct model over the incorrect one. Therefore, a good model selection indicator is the one that increases the fastest when F_0 is increased.

From Figure 1, we see that the RMSE selects the correct model over the incorrect one given by $F_0 = 8.1$ with a probability of 0.25 that is slightly inferior to the G-CME probability of 0.27. As the forcing of the incorrect model increases, both indicators increase their probabilities of selection but the growth of the G-CME indicator is faster.

ROC curves and the Gini coefficient. The probabilities of selection as computed in Figure 1 only evaluate the ability of the indicators to select one model over the other. Yet the values of these indicators also provide distances between the two models. The greater these distances, the greater the confidence in the corresponding model selection.

We define the confidence value in the model selection for the G-CME indicator as the difference between the logarithms of the model evidences, introduced in section 2, namely

$$\Delta_{\text{G-CME}} = \ln\{p_1(\mathbf{y})\} - \ln\{p_0(\mathbf{y})\}, \quad (20)$$

with p_1 being the G-CME value for the correct model and p_0 the G-CME value for the incorrect one. Similarly, a confidence value

is defined for the RMSE, as

$$\Delta_{\text{RMSE}} = \text{RMSE}_0 - \text{RMSE}_1, \quad (21)$$

with RMSE_1 , defined in Eq. (19), for the correct model and RMSE_0 for the incorrect one.

In order to evaluate the ability of each indicator to select the correct model with various levels of confidence, we compute a Receiver Operating Characteristic (ROC) curve. A ROC curve measures the performance of a binary classifier; see, for instance, Metz (1978) for a review of ROC analysis.

In our study, we define the ROC curve as follows. If the confidence value Δ (either $\Delta_{\text{G-CME}}$ or Δ_{RMSE}) is positive, we consider the correct model to have been selected and the incorrect one if it is negative. Knowing that there is only one correct model, we define the selection of the latter as a true positive instance and the selection of the incorrect model as a false positive instance.

Note that, with this definition of the classifier, there is neither a true negative nor a false negative for which a confidence value is obtained. Still, this configuration allows us to define the True Positive Rate (TPR) and the False Positive Rate (FPR), two parametric functions of the threshold $\Xi \in [0, 1]$, giving the proportion of positives that are correctly identified as such (i.e., when $\Delta > \Xi$) and, respectively, the proportion of negatives wrongly identified as positives (i.e., when $-\Delta > \Xi$). The ROC curve is then displayed by plotting parametrically the $\text{TPR}(\Xi)$ against the $\text{FPR}(\Xi)$ for varying thresholds Ξ .

The random classifier has a 50% chance of selection of each model for every threshold and it will produce a diagonal ROC curve (black dashed line in Figure 2, 4 and 6), namely a straight line between the origin (0, 0) and the point (1, 1), while a perfect classifier that always selects the correct model corresponds to a ROC curve equal to 0 for $\Xi = 0$ and to 1 for $\Xi \in (0, 1]$.

Figure 2 shows the ROC curves of the model selection indicator RMSE (solid red line with red circles) and the model selection indicator G-CME (solid green line with squares), for two incorrect models: (a) the one closest to the correct value, i.e. $F_0 = 8.1$; and (b) and the one farthest from it, i.e. $F_0 = 8.9$. Both indicators outperform random selection by exhibiting a higher TPR/FPR ratio throughout, for every threshold Ξ . Similarly to the

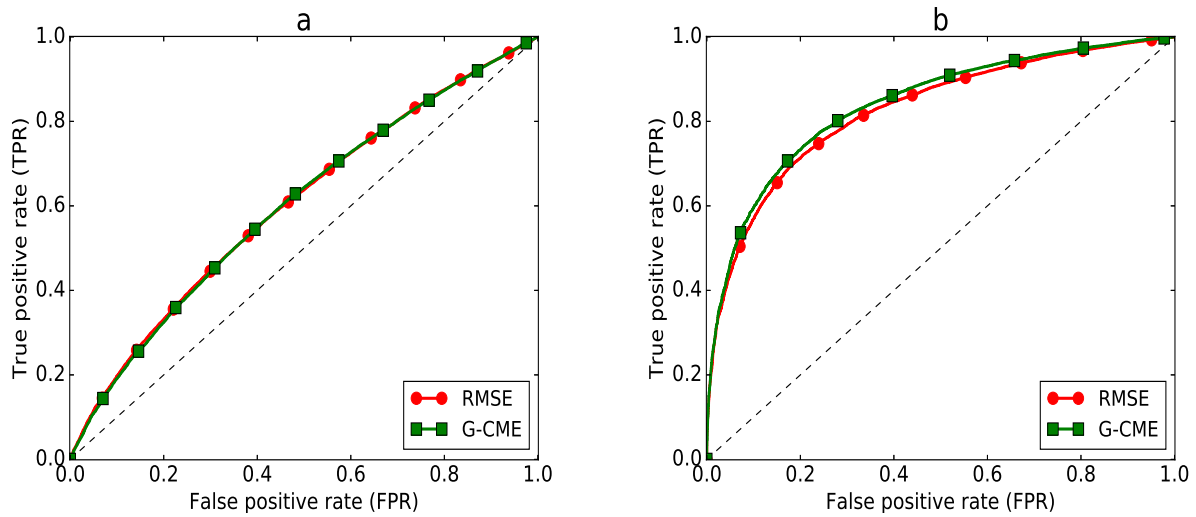


Figure 2. ROC curves of the two model selection indicators, RMSE and G-CME between the correct model, with $F_1 = 8$, and two of the incorrect models, with (a) $F_0 = 8.1$, and (b) $F_0 = 8.9$, both for a 40-member ensemble. The two curves, for RMSE and G-CME, use the same lines as in Figure 1.

probability of selection in Figure 1, the RMSE and the G-CME are almost equally selective for the more difficult case of the incorrect model $F_0 = 8.1$ in panel (a), while the G-CME indicator slightly outperforms the RMSE for $F_0 = 8.9$ in panel (b).

The Gini coefficient γ (Gini 1921) provides a simple scalar that quantifies the improvement of a given classifier over the random one. This coefficient equals the area A between the classifier's ROC curve and the diagonal of the graph — which is the ROC curve of the random classifier — divided by the area between the latter and the x -axis. In other words, $\gamma = A/(1/2) = 2 \times A$. Hence, the Gini coefficient for the random classifier is 0 and the Gini coefficient for a perfect classifier is 1.

	RMSE	G-CME
$F_0 = 8.1$	0.205	0.202
$F_0 = 8.9$	0.652	0.680

Table 1. Gini coefficients of the model selection indicators obtained using the RMSE and the G-CME between the correct model, with $F_1 = 8$, and the two incorrect models, with $F_0 = 8.1$ and $F_0 = 8.9$, computed for a 40-member ensemble. These Gini coefficients are based on the ROC curves in Figure 2.

The Gini coefficients corresponding to the ROC curves in Figure 2 are reported in Table 1. In the case of the incorrect model with $F_0 = 8.1$, the Gini coefficients of the RMSE and the G-CME are very close, with only a 0.003 difference in favor of the RMSE. The G-CME outperforms the RMSE in the case of the incorrect model with $F_0 = 8.9$: its Gini coefficient is higher by 0.028.

To summarize, results so far suggest that the G-CME and the RMSE present comparable selection skills for similar models,

such as in the case $F_1 = 8$ and $F_0 = 8.1$, but the G-CME converges faster to a perfect classifier as F_0 is increased.

4.2.2. CME with domain localization

In the previous subsection, a 40-member ensemble was used to compute the model selection indicators. However, in geosciences applications, such a big ensemble, with N comparable to the state vector size M , is quite unrealistic. To mimic a more realistic scenario, we use here a 10-member ensemble, i.e. $N \ll M = 40$, in conjunction with localization. Bocquet and Carrassi (2017) have shown that $N = 10$ is smaller than the dimension of the unstable–neutral subspace below which localization is mandatory.

Here we use the localization radius $\rho_{\text{loc}} = 5$, as it produces the smallest RMSE^t for the DA process applied to the incorrect models (not shown here). Since the localization is tuned for the incorrect model–DAs, but left untuned for the correct–model DA, the analysis errors of the two DAs should be closer to each other than if the localization were tuned independently for each model. This choice is expected to render the model selection task harder.

We compare then the selectivity of the DL-CME to the G-CME and the RMSE. Note that unless stated otherwise the same 10-member ensemble is used to compute the three model selection indicators: DL-CME, G-CME and RMSE. As before, these three model selection indicators are computed at each of the $T = 5 \times 10^4$ cycles of the numerical experiment.

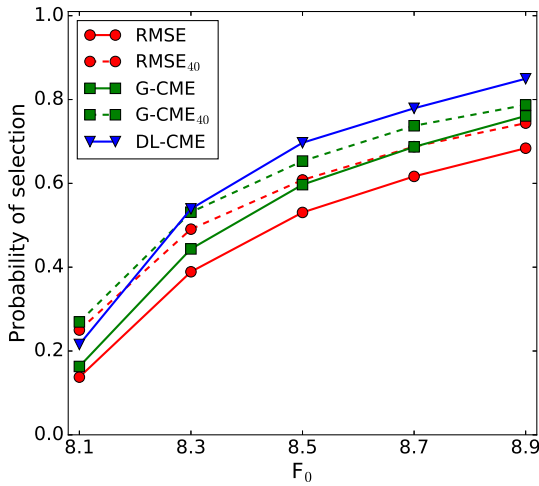


Figure 3. Same as Figure 1, but including now the DL-CME model selection indicator, with a localization radius of $\rho_{loc} = 5$, shown as the solid blue line with triangles. All three solid lines correspond to a 10-member ensemble, while the results from Figure 1 for the RMSE and the G-CME that were computed for a 40-member ensemble are plotted here as dashed; see also the figure's legend.

Probability of selection. Figure 3 shows the probabilities of selection as a function of the incorrect models, with $F_0 > F_1$, for three model selection indicators: RMSE, G-CME and DL-CME. The probabilities for the RMSE and the G-CME using the 40-member ensemble, and displayed in Figure 1, are also reported in Figure 3 for comparison.

First, we note that the probabilities of selection for both RMSE and G-CME are lower for $N = 10$ than for $N = 40$. This means that the use of a smaller ensemble and no localization in the DA reduces the probabilities of a correct selection by the RMSE and the G-CME and is a direct consequence of the reduced accuracy of the DA in performing the state estimate. However, the convergence rate of the G-CME with $N = 10$ is faster than for G-CME₄₀ and, when $F_0 = 8.9$, they select the correct model with almost the same accuracy.

The key result, though, is related to the effect of localization. We see that for the same ensemble size $N = 10$, the DL-CME outperforms both the RMSE and the G-CME indicators. Notably, the DL-CME with $N = 10$ selects the correct model with a higher probability than the G-CME with $N = 40$, except for the case of smallest error in model definition, i.e. for $F_0 = 8.1$.

ROC curves and the Gini coefficient. The previous conclusion is confirmed by the ROC curves in the cases of the incorrect models with $F_0 = 8.1$ and $F_0 = 8.9$ that are plotted, respectively,

in Figures 4(a, b). The ROC curves of G-CME₄₀ have also been plotted in Figure 4 for reference and benchmark. The DL-CME has a TPR/FPR ratio that is larger than the G-CME for both incorrect models. This result represents a substantial improvement in the computation of the CME.

In the difficult case of $F_0 = 8.1$, the DL-CME with $N = 10$ is not as accurate in model selection as the G-CME₄₀ but, as previously stated, the use of large ensembles is most often not feasible for models of a realistic size. Interestingly, in the case of $F_0 = 8.9$, the DL-CME still provides a more accurate model selection than the G-CME₄₀.

These results are confirmed by the corresponding Gini coefficient listed in Table 2. In the case $F_0 = 8.9$, the DL-CME model selection skill outperforms the G-CME₄₀, even though the DA performance for state estimation in terms of RMSE^t is better when $N = 40$ with no localization than $N = 10$ with localization (not shown).

	RMSE	G-CME	DL-CME	G-CME ₄₀
$F_0 = 8.1$	0.102	0.097	0.154	0.202
$F_0 = 8.9$	0.590	0.656	0.748	0.680

Table 2. Same as Table 1, for the four ROC curves in Figure 4.

4.2.3. Sensitivity to the localization radius

Even though only the DL-CME takes into account the localization, the G-CME and the RMSE are also potentially sensitive to the localization radius since they are based on the output of a DA cycle that uses localization. The way the three model selection indicators respond to the localization radius ρ_{loc} is examined in Figure 5.

The experimental setup is identical to that in the previous subsections and the ensemble size is $N = 10$. The localization radius ρ_{loc} is shown on the x -axis; while the Gini coefficient for each model selection indicator is plotted on the y -axis. Superimposed on Figure 5 are the RMSE^t curves for the DA with the correct and the incorrect model, in solid and dashed black lines, respectively.

The results in Figure 5 confirm, once more, the superiority of the two CME indicators over the RMSE. They also confirm the

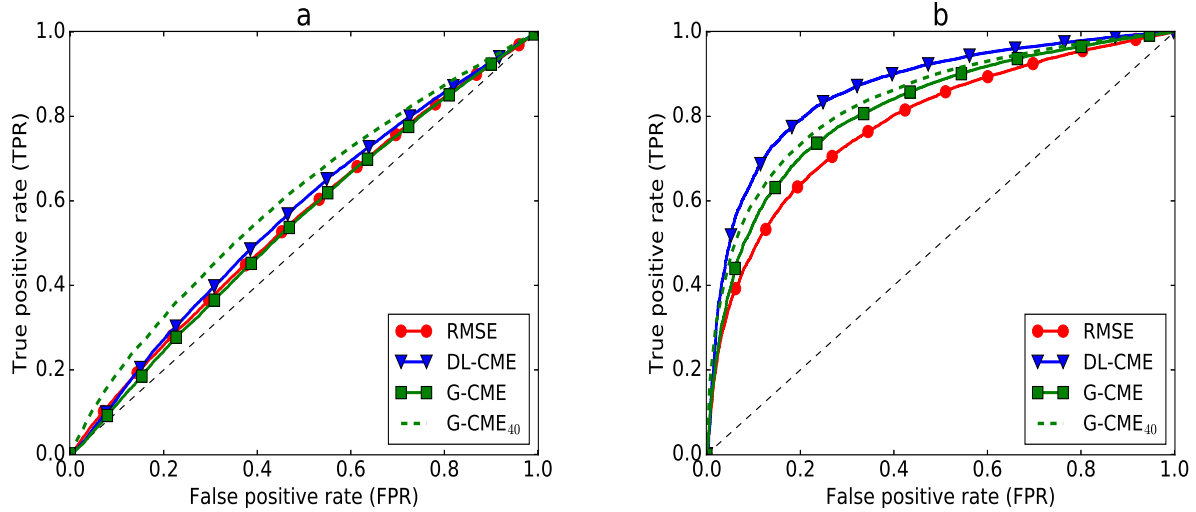


Figure 4. ROC curves of four model selection indicators plotted in Figure 3. The RMSE (solid red line with circles), G-CME (solid green line with squares) and DL-CME (solid blue line with triangles) all use a small ensemble with $N = 10$, while the G-CME₄₀ (dashed green line) uses a larger, 40-member ensemble. As in Figure 2, the ROC curves evaluate the skill at distinguishing between the correct model, with $F_1 = 8.0$, and two of the incorrect models: (a) with $F_0 = 8.1$, and (b) with $F_0 = 8.9$. As in Figure 2, the DL-CME uses a localization radius of 5.

improvement achieved by taking into account domain localization in the CME computation, i.e., the better model selection by the DL-CME with respect to the G-CME; both improvements are present across all localization radii.

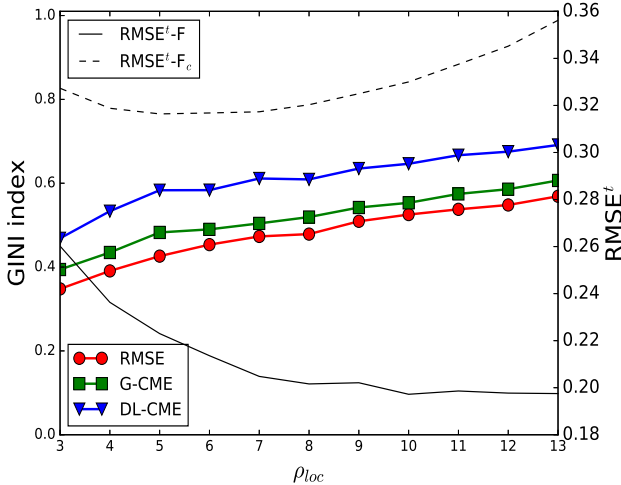


Figure 5. Gini coefficients of the three model selection indicators between the correct model, with $F_1 = 8.0$ and the incorrect model with $F_0 = 8.5$: RMSE, G-CME, and DL-CME; each of the three indicators is plotted using the same curve styles as in Figure 4. The results are for a 10-member ensemble and the varying localization radius ρ_{loc} is shown on the x -axis. The solid black line and the dashed black line represent the RMSE^t scores for the correct and the incorrect models, labeled as F_1 and F_0 , respectively.

It is, moreover, worth noting that the sensitivity of all three indicators to the localization radius is small. For all the indicators, the Gini coefficient increases slowly with ρ_{loc} . This increase can be explained by the difference in performance of the DA's state estimation. Indeed the difference between the two RMSE^t curves

also increases with the localization radius. Hence, the selection between the two DA-produced ensembles becomes easier as ρ_{loc} increases. The key result, however, is that the sensitivities of the two CME indicators are approximately the same. Thus, taking the localization into account in the CME computation should improve the CME's model selection skill, whatever the value of the localization radius.

4.2.4. Dependence on the evidencing window

In all previous experiments, the model selection indicators are computed over an evidencing window $K = 1$, i.e., using only one DA cycle. This choice was made to assess the indicators' performance in the most difficult setting. Indeed, selecting a model based on static information alone is a difficult task that is not usually required in geosciences applications. In the latter, one may want to select the most accurate model representation of a meteorological event or a climatological time span, seen as a “video loop” or a “full-length movie”, respectively (Ghil 1997). We thus want now to evaluate the indicators in a more realistic setting, by comparing the correct model, with $F_1 = 8.0$, and the most incorrect one being considered, with $F_0 = 8.9$, over larger evidencing windows, namely $K = 2$ and $K = 4$.

The ROC curves obtained for these two experiments, with $K = 2$ and $K = 4$, are displayed in Figures 6(a) and (b), respectively. Comparing these curves with these for $K=1$ of Figure 4(b),

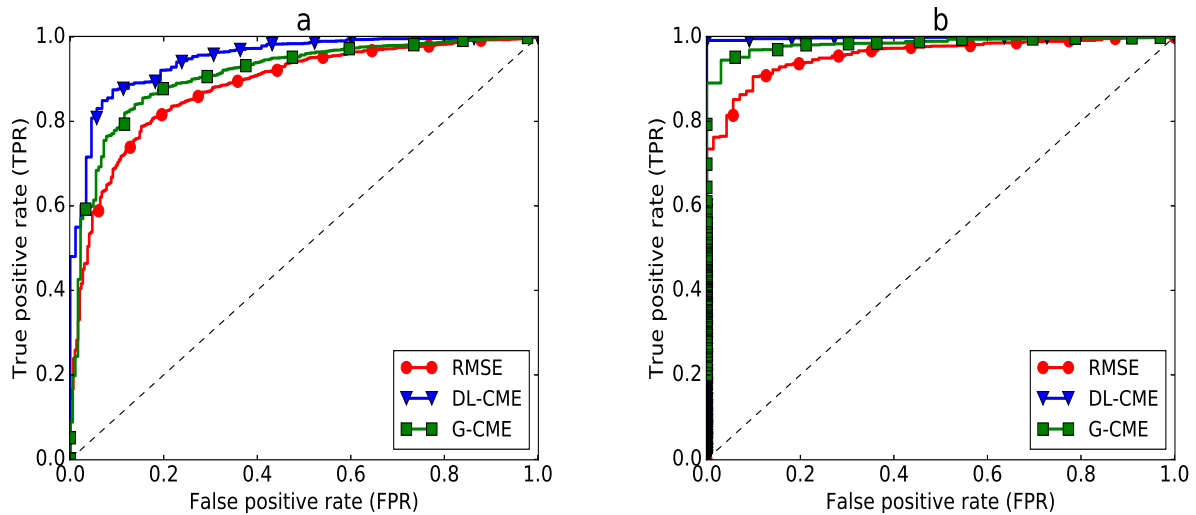


Figure 6. Same as Figure 4(b), but for a longer evidencing window and using only a 10-member ensemble: (a) $K = 2$, and (b) $K = 4$.

we see that increasing the evidencing window improves the selection skills of all the indicators as they converge to the perfect classifier. This behavior is consistent with the results obtained by Carrassi et al. (2017) in the absence (of the need) of localization.

Moreover, in the case $K = 2$, the DL-CME still outperforms the RMSE and the G-CME. In the case $K = 4$, both CME indicators remain more accurate than the RMSE, while the DL-CME is almost achieving a perfect selection. Altogether, the results in Figures 4(b), 6(a) and 6(b) indicate that when K is increased all indicators converge to the perfect classifier. It follows that, for small and medium evidencing windows, the DL-CME outperforms the CME with no localization and the RMSE, but larger evidencing windows, when feasible computationally, may allow all indicators to show similar selection skills.

5. Numerical experiments with an atmospheric model

This section presents the first implementation of the CME approach for an intermediate-complexity model. The numerical experiments herein confirm the benefits of applying CME in general, and DL-CME in particular, as a model selection indicator for larger models.

5.1. Experimental setup

5.1.1. The SPEEDY model

We use an atmospheric general circulation model (AGCM) based on a spectral primitive-equation dynamic core that resolves the large-scale dynamics of the atmosphere. The

model was developed at the International Center for Theoretical Physics (ICTP) and it is referred to as the ICTP AGCM or the Simplified Parameterizations, primitive-Equation Dynamics (SPEEDY) model (Molteni 2003; Kucharski 2006). With its dynamical core and its simplified physical parameterization schemes, SPEEDY simulates successfully some of the complex physics described by state-of-the-art AGCMs, while maintaining a low computational cost (Neelin et al. 2010). Hence, its intermediate-level complexity — between low-order models and high-end AGCMs — has made SPEEDY an important test bed for model development studies (e.g., Kucharski 2003; Haarsma 2003; Bracco 2004; Kucharski 2006) and for evaluating DA methodology (Miyoshi 2005; Miyoshi and Yamane 2007).

The model's spectral dynamical core (Molteni 2003) uses a hydrostatic, σ -coordinate, spectral-transform formulation in the vorticity-divergence form described by Bourke (1974). The configuration we use here is described by Miyoshi (2005) and it has a spectral resolution of T30L7, i.e., a horizontal spectral truncation at spherical wavenumber 30 and 7 vertical layers. It has a vertical σ -coordinate and it computes four physical variables in every vertical layer: zonal wind u , meridional wind v , temperature T , and relative humidity q , as well as one surface variable, in the lowest vertical layer, namely surface pressure p_s .

The simulated values for each vertical field are given on a $96 \text{ long.} \times 48 \text{ lat.}$ horizontal grid. A summary description of SPEEDY, including its simplified physical parametrizations, is available in the appendix of Molteni (2003). We provide here a

detailed description of its convection parametrization, since the purpose of the present section is to perform parameter selection between two values of a convective parameter.

5.1.2. The model's convection parametrization

SPEEDY's convection scheme is a simplified version of the mass-flux scheme developed by Tiedke (1993). The scheme simulates the balance of the updraft of the saturated air and the large-scale downward motion in between the planetary boundary layer (PBL) and the top-of-convection (TCN) layer. While the updraft of saturated air is triggered above the PBL, the detrainment only takes place in the TCN layer. In addition, the convection scheme simulates an exchange of moisture between the PBL and the layers above it.

SPEEDY's simplified convection parametrization may roughly be summarized by three main steps: an activation of the convection scheme, its closure and an exchange mechanism between the intermediate layers. In particular, the closure of the scheme requires the convective moisture tendency in the PBL to be equivalent to a relaxation of humidity towards a prescribed threshold with a relaxation time equal to τ_{cnv} ; in our study, the parameter of interest is precisely τ_{cnv} . This parameter has a straightforward physical interpretation since it controls the speed of the vertical mixing associated with moist convection, and its interest lies in its impact on the global-scale circulation.

The correct parameter value, namely the value set in SPEEDY to create a 'true' trajectory — in the sense defined in sections 2 and 4 — is $\tau_{\text{cnv}} = 6$ hr. Meanwhile, the incorrect parametrization here will use the relaxation time $\tau_{\text{cnv}} = 9$ hr. The objective is to be able to select the correct parameter over the incorrect one, based on the observation of what is deemed to be the true trajectory in the present, "dizygous-twin" setting; see, for instance, Ghil and Malanotte-Rizzoli (1991) for an explanation of the distinctions between identical-twin, dizygous-twin and real-observations setup in DA studies. The DA formulation needed to do the parameter selection in this setup is presented in the next subsection.

5.1.3. The DA implementation

As in the L95 experiments of section 2, a true trajectory \mathbf{x}^t is generated using the correct parameter value of $\tau_{\text{cnv}} = 6$ hr. From this trajectory a set of observations are derived and made available every 6 hr. This DA configuration was adapted for SPEEDY by Miyoshi (2005).

The observed physical quantities are the 5 prognostic variables u , v , T , q , throughout the model's 7 layers, and the surface pressure p_s . All variables are observed every four gridpoint, yielding $(96 \times 48 \times 7)/8 = 4032$ observations for u , v , T , q and $(96 \times 48)/8 = 576$ observations for the surface pressure. The observation error variances, used to create the observations in the DA process, are:

$$\begin{aligned}\sigma_u &= \sigma_v = 1 \text{ m.s}^{-1}, \\ \sigma_T &= 1^\circ \text{C}, \\ \sigma_q &= 1 \text{ g.kg}^{-1}, \\ \sigma_{p_s} &= 1 \text{ hPa}.\end{aligned}$$

The experiment lasted 6 months, from 1 January to 30 June 1983. The results for the spin-up time of $T_{\text{su}} = 124$ DA cycles (i.e., the 1st month) were discarded, and the diagnostics were calculated for the $T = 600$ DA cycles of 1 February through 30 June.

The DA is performed using the LETKF (cf. Sect. 3.1.2) with $N=50$ ensemble members and with the domain localization introduced by Hunt et al. (2007), Miyoshi and Yamane (2007), and Greybush et al. (2011): localization domains are selected and the observation error covariance sub-matrix $\mathbf{R}|_s$ is multiplied, for each $s \in \Gamma$, by the inverse of a smoothing function, as explained in section 3.1. In this study, we use the implementation proposed by Miyoshi et al. (2007) and apply as a smoothing function, in the three-dimensional physical space, the Gaussian function

$$\phi(r) = \exp\left(\frac{-r^2}{2\rho_{\text{loc}}^2}\right); \quad (22)$$

here r is the distance between the localization domain's center and the observations, while ρ_{loc} is the localization radius, and both quantities have a horizontal and a vertical component. The horizontal component of ρ_{loc} is taken equal to 700 km, while its

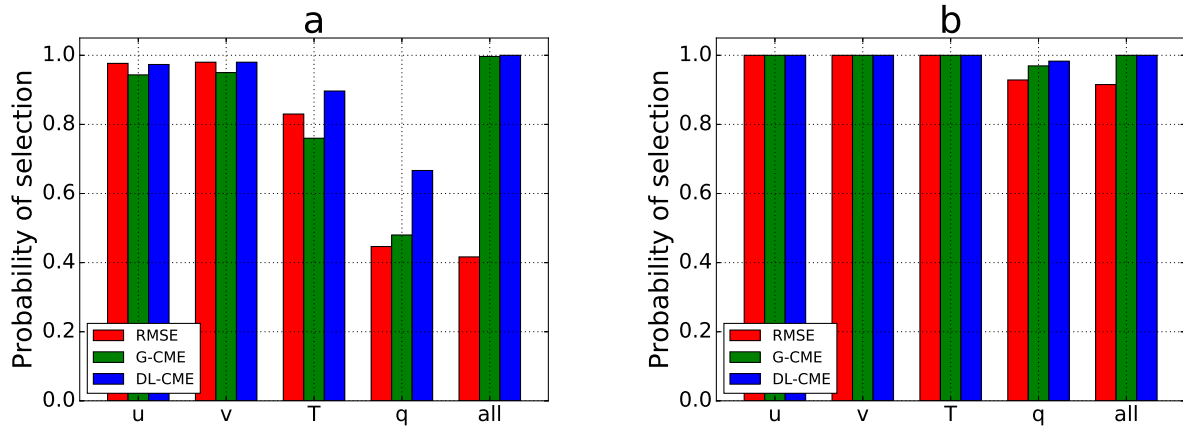


Figure 7. Probability of selection of the correct parameter value over the incorrect one, obtained by using three model selection indicators: RMSE (red bar on the left), the G-CME (green bar in the middle) and the DL-CME (blue bar on the right). The results are given for the variables u , v , T , q , and for all variables ('all'); the evidencing window has length (a) $K = 1$, and (b) $K = 12$.

vertical component is defined in terms of log-pressure coordinates and corresponds to approximately 4 km.

Note that, in the following, the DL-CME results are computed for specific variables, i.e., we assume that only these variables have been observed. This computation is identical to the computation of the CME for an observation subvector, as discussed in section 3.2.1.

For an evidencing window that has length $K \geq 2$, the required computation of the pdf of the system's state, conditioned on this particular observation subvector leads to a DA run that does not converge. Hence, we approximate once again this conditional pdf by the original posterior pdf which consists in directly applying the EnKF-formulation to the observation vector reduced to a specific variable using Eq. (14).

5.2. Model selection problem

We now focus, as explained in section 5.1.2, on determining which value of the relaxation parameter τ_{cnv} (6 or 9 hrs) is more appropriate to describe the atmospheric evolution simulated during the 5 months of the experiment. Recall that the value $\tau_{\text{cnv}} = 6$ hrs is the one used to simulate the reference truth from where the observations are sampled. The model selection is here a parameter identification problem and, again, is carried out with the RMSE, the G-CME, and the DL-CME as indicators.

The indicators are first computed on the evidencing window $K = 1$, i.e., on a single DA cycle then averaged over the 5-month interval. The results in terms of selection probability obtained on the various variables are shown in Figure 7(a).

As mentioned in section 5.1.2, the value of the relaxation time τ_{cnv} plays an important role in the global-scale circulation: it intensifies, for instance, the mesoscale circulations associated with deep convection which then affects the extent and intensity of the Hadley and Walker cells (see for instance Donner et al. 2001). This physical connection is confirmed by the results of the three model selection indicators when using observations of the variables u or v alone. Indeed, for either of these two variables, the indicators select the correct parameter with high probability. Though, it is to be noted that the RMSE outperforms the G-CME selecting skills on these two variables. However, taking into account localization, i.e., using the DL-CME, improves the selection skills of the CME and provides equally high selection probabilities as the RMSE does. Moreover, when only T-data are used, the DL-CME identifies the correct parameter with the highest probability. The humidity variable, q , is the variable least impacted by the variation of τ_{cnv} . Yet, the DL-CME is the best to emphasize the improvement of the correct parameter on the humidity representation. Finally, when using all observations, both CMEs fully discriminate between the two models whereas the RMSE only partially does. A more realistic setting is to use a longer evidencing window, taken now as $K = 12$, which corresponds to 3 days. The results of this experiment are shown in Figure 7(b), and they confirm that increasing K improves the selection skills of all indicators. The humidity is still the most difficult variable to discriminate the two models from. Yet, the DL-CME remains the best selector, strongly selective for all variables, both separately and together. Moreover, when using

all observations, the RMSE fails to systematically recognize the correct model from the incorrect one.

From a practical stand-point, the latter result indicates that if, for instance, one's goal is to determine which of two models is most likely responsible for a three-day weather event that was fully observed, the DL-CME is more likely than the RMSE to provide the correct answer.

5.3. Mapping model evidence

Local CMEs, defined by Eq. (14), also provide a spatial representation of model evidence. This is exploited in Figure 8 that shows the spatial differences between the correct and the incorrect parametrization using all observations.

Note that the distinct information conveyed by these two maps — the local RMSE differences in panel (a) and the local CME differences in panel (b) — is not necessarily contradictory but rather complementary since the RMSE is the Euclidean distance between the DA forecast and the observations while the local CME can be seen as a distance between the same two quantities but smoothed by the uncertainties that surround them.

Indeed, the local RMSE reveals a significant difference between the two models all over the globe while the local CME shows that this difference mainly impacts the low latitude regions. Also, some of the regions that are strongly impacted by the incorrect parameter according to the RMSE, are not so according to the local CME. For instance, the differences emphasized by the RMSE in the region off the coast of China are sensibly smaller according to the local CMEs. This would suggest that, although the DA forecast produced by the incorrect model does not fit the observations as well as the one produced by the correct model, the uncertainties generated in this region mitigate the quality of the correct model's representation of this region.

6. Concluding remarks

6.1. Summary and conclusions

Carrassi et al. (2017) have introduced the contextual model evidence (CME) as a powerful indicator for model selection and for attribution of climate related events. They have also have

provided analytic ways to compute this indicator by using a hierarchy of ensemble-based data assimilation (DA) algorithms and have shown its efficiency.

When applied to large-dimensional models, ensemble-based DA requires localization techniques in order to mitigate the spurious effect of under-sampling. The present study focused on adapting the CME's EnKF-formulation to the use of a specific localization technique, namely domain localization.

In section 3.2.1, we have shown how to compute local CMEs as the CMEs of an observation subvector. This idea led to an EnKF-formulation of the local CME, given by Eq. (14), subject to very few simplifying assumptions. Combining local CMEs for each grid point, we introduced in Eq. (15) a heuristic model selection indicator called the domain-localized CME (DL-CME). This DL-CME formulation allows one to estimate model evidence in a consistent and routine way by using localized DA with large-dimensional problems.

We implemented the DL-CME formulation — along with the global CME's EnKF-formulation called global CME (G-CME) and the root mean square error (RMSE), defined by Eq. (19) — on two atmospheric models: the Lorenz 40-variable mid-latitude atmospheric dynamics model (L95: Lorenz and Emanuel 1998) and the simplified global atmospheric SPEEDY model (Molteni 2003), in sections 4 and 5, respectively. The main objective of the numerical experiments in these two sections was to assess the performance of the three approaches so defined — the RMSE, the G-CME and the DL-CME — in increasingly harder model selection problems.

In section 4, the numerical experiments based on the L95 model were used to compare the three model selection indicators for varying model forcings F , as well as with respect to the localization radius ρ_{loc} and to the length K of the evidencing window. In general, both CME indicators, G-CME and DL-CME, are more accurate than the RMSE; see Figures 1–6. Moreover, the DL-CME outperforms systematically the G-CME regardless of the length of the localization radius, cf. Figure 5.

In the 40-ensemble member localization-free experiment, the G-CME increasingly outperforms the RMSE when the difference between the model forcings is increased; see Figures 1–2. When the number of ensemble members is reduced to 10, hence making

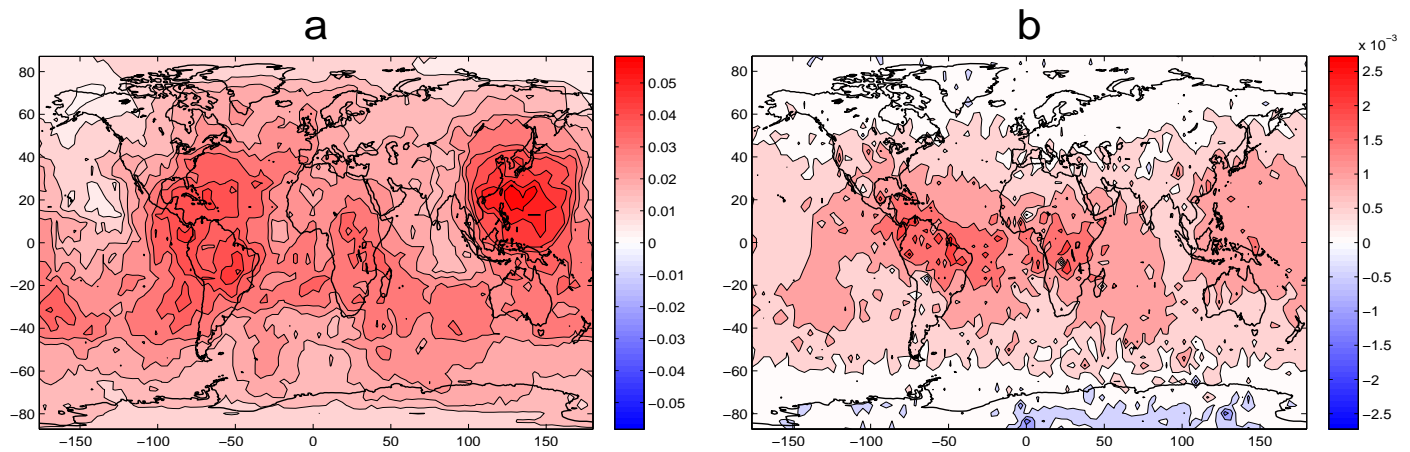


Figure 8. Spatial difference between the model with the correct and incorrect parameter values, shown for humidity q and $K = 1$, and averaged over the 5-month interval. (a) RMSE results, and (b) DL-CME results.

localization necessary, the G-CME is still more accurate than the RMSE. With the same ensemble size, the DL-CME is even more accurate than the G-CME which indicates the impact of consistently using localization in both the DA state estimation procedure and in the CME computation. Remarkably, DL-CME, with a 10-member ensemble and localization, produces better selection probabilities than G-CME with a 40-member ensemble and no localization, at least when the discrepancy between the correct and incorrect forcing is large enough, cf. Figures 3-4.

The sensitivity of the model selection skills to the localization radius is approximately the same for all indicators, meaning that the improvement of the DL-CME over the two other indicators is almost independent of the localization radius, cf. Figure 5. This independence is highly desirable, given the computational cost of tuning the radius. In particular, the DL-CME is clearly the most accurate indicator for small evidencing windows. For larger windows, the performances of the DL-CME and the G-CME become almost identical and do remain higher than the RMSE's performance, see Figure 6.

In section 5, model selection was carried out for a more realistic problem. We formulated two parametrizations of the convection in the SPEEDY model by varying the convective relaxation time τ_{cnv} . The selecting skills of the RMSE, the G-CME and the DL-CME were assessed on all physical model variables, both separately and together.

Over a single DA-cycle, the DL-CME and the G-CME are fully selective on all variables combined. The DL-CME, though, is the best selection indicator on all four model variables — u , v , T and q

— separately, whether for a single DA-cycle or a large evidencing window, $K = 12$, as shown in Figure 7.

Local CMEs provide, in addition, a spatial view of model evidence, cf. Figure 8. This spatial view can provide precious information on the impacts of the correct and incorrect parametrizations on the physical evolution of the large-scale atmospheric flow.

In summary, while the DL-CME displays the best performance in terms of model selection, the spatial plots of local CME can help identifying the spatial regions and the physical variables where the incorrect model misfits the observations. Beyond model selection problems, this feature can be used to bring precious information in order to help understanding the causal chain leading to meteorological or climatological events as well as designing target observations/areas for that purpose.

6.2. Future directions

A first line of future investigations should focus on strengthening the theoretical foundation of the CME. Indeed, several theoretical issues are yet to be addressed. For instance, simulating model error and taking it into account in both the DA process and in the CME computation could improve significantly the CME's model selection skill. The DA community is still conducting active research on the best ways to incorporate model error in DA methodology (e.g., Dee 1995; Raanes et al. 2015; Carrassi and Vannitsem 2016; Harlim 2017). This research has the potential to improve significantly the accuracy of the DA product improving therewith the CME estimation. Moreover,

taking into account model error in the CME computation itself could also have an impact in the CME's model selection abilities.

Another theoretical issue requiring investigation is the derivation of an exact global indicator based on local CMEs that could outperform the global heuristic indicator proposed in this article, the DL-CME. These theoretical challenges are part of the authors' current research program.

A second line of investigations should focus on broadening the applications of the CME approach by increasing the realism and the complexity of the models considered, on the one hand, and by widening the use of the CME from model selection to other purposes like event attribution for example, on the other hand. In particular, it seems worth investigating the potential of the spatial representation of local CMEs for diagnosing causality in a geoscientific system, as proposed by Hannart et al. (2016b).

Acknowledgments

We acknowledge discussions with the other members of the DADA team (Philippe Naveau, Aurélien Ribes and Manuel Pulido). We also wish to acknowledge the personal communications with Pr. P.J. Van Leeuwen which led to significant clarifications of the manuscript.

This research was supported by grant DADA from the Agence Nationale de la Recherche (ANR, France: All authors), and by Grant N00014-16-1-2073 of the Multidisciplinary University Research Initiative (MURI) of the US Office of Naval Research (MG). A. Carrassi has been funded by the Nordic Centre of Excellence Embla of the Nordic Countries Research Council, NordForsk, and by the project REDDA of the Norwegian Research Council (contract number 250711). CEREa is a member of the Institute Pierre Simon Laplace (IPSL).

Appendix A

Alternative implementation of the global CME (G-CME)

The G-CME implementation was first presented in Carrassi et al. (2017) for the CME formulation based on the En-4D-Var DA method. This implementation makes the assumption that the observation error covariance matrix \mathbf{R} is diagonal. This assumption is strong but often verified in geosciences applications.

Implementing Eq. (8) requires to derive: (i) the determinant term $|\Sigma_k|$; (ii) the weighted sum of squares $(\mathbf{y}_k - \mathbf{H}_k \mathbf{x}_k^f)^T \Sigma_k^{-1} (\mathbf{y}_k - \mathbf{H}_k \mathbf{x}_k^f)$. We deal with each two terms separately.

First, the computation of the determinant term can be greatly simplified by application of Sylvester's determinant rule (i.e., $|\mathbf{I} + \mathbf{AB}| = |\mathbf{I} + \mathbf{BA}|$ for any two rectangular matrices \mathbf{A} and \mathbf{B} of conformable sizes). We have

$$\begin{aligned} |\Sigma_k| &= |\mathbf{H}_k \mathbf{P}_k^f \mathbf{H}_k^T + \mathbf{R}| \\ &= |\mathbf{R}| \cdot |\mathbf{I}_d + \mathbf{R}^{-\frac{1}{2}} \mathbf{H}_k \mathbf{P}_k^f \mathbf{H}_k^T \mathbf{R}^{-\frac{1}{2}}| \\ &= |\mathbf{R}| \cdot |\mathbf{I}_N + \Delta_k| \end{aligned} \quad (23)$$

where $\Delta_k = (\mathbf{x}_k^f)^T \mathbf{H}_k^T \mathbf{R} \mathbf{H}_k \mathbf{x}_k^f$. with \mathbf{x}_k^f , the normalized forecast anomalies such that $\mathbf{x}_k^f (\mathbf{x}_k^f)^T = \mathbf{P}_k^f$. Note that \mathbf{R} is diagonal in general thus its determinant is easy to compute.

Under Eq. (2), one sees that $|\Sigma_k|$ boils down (after the one off computation of $|\mathbf{R}|$) to the computation of $|\mathbf{I}_N + \Delta_k|$ which is a much smaller determinant of dimension N (size of the ensemble) instead of dimension d (size of the observation vector).

Second, the computation of the weighted sum of squares can also be greatly simplified by application of the Sherman-Morrison-Woodbury formula. We have

$$\begin{aligned} \Sigma_k^{-1} &= (\mathbf{H}_k \mathbf{P}_k^f \mathbf{H}_k^T + \mathbf{R})^{-1} \\ &= (\mathbf{H}_k \mathbf{x}_k^f (\mathbf{x}_k^f)^T \mathbf{H}_k^T + \mathbf{R})^{-1} \\ &= \mathbf{R}^{-1} - \mathbf{R}^{-1} \mathbf{H}_k \mathbf{x}_k^f (\mathbf{I}_N + \Delta_k)^{-1} (\mathbf{x}_k^f)^T \mathbf{H}_k^T \mathbf{R}^{-1} \end{aligned} \quad (24)$$

It follows

$$\begin{aligned} &(\mathbf{y}_k - \mathbf{H}_k \mathbf{x}_k^f)^T \Sigma_k^{-1} (\mathbf{y}_k - \mathbf{H}_k \mathbf{x}_k^f) \\ &= (\mathbf{y}_k - \mathbf{H}_k \mathbf{x}_k^f)^T \\ &(\mathbf{R}^{-1} - \mathbf{R}^{-1} \mathbf{H}_k \mathbf{x}_k^f (\mathbf{I}_N + \Delta_k)^{-1} (\mathbf{x}_k^f)^T \mathbf{H}_k^T \mathbf{R}^{-1}) \\ &(\mathbf{y}_k - \mathbf{H}_k \mathbf{x}_k^f) \\ &= (\mathbf{y}_k - \mathbf{H}_k \mathbf{x}_k^f)^T \mathbf{R}^{-1} (\mathbf{y}_k - \mathbf{H}_k \mathbf{x}_k^f) - \mathbf{v}_k (\mathbf{I}_N + \Delta_k)^{-1} \mathbf{v}_k^T \end{aligned} \quad (25)$$

with $\mathbf{v}_k = \mathbf{R}^{-1} \mathbf{H}_k \mathbf{x}_k^f$.

Under Eq. (24) and (25), one sees that the second term boils down (after the one off inversion of \mathbf{R}) to the inversion of $\mathbf{I}_N + \Delta_k$, which again is a much smaller matrix of dimension N instead

of dimension d , and to the computation of the intermediate vector \mathbf{v}_k of dimension N .

Appendix B

Derivation of the CME formulation using covariance localization

Covariance localization (also called Schur localization) consists in restraining the spatial impact of the empirical forecast error covariances. Indeed, the ensemble size is smaller than the model's state dimension and thus the ensemble-based covariance is subsampled by construction. This subsampling may lead to spurious correlations. This issue can be partly overcome by removing the unrealistic correlations. Covariance localization performs this removal by applying to the forecast error covariance matrix \mathbf{P}_f a Schur product (i.e., a pointwise multiplication) with a smoothing correlation matrix \mathbf{C}

$$[\mathbf{C} \circ \mathbf{P}_f]_{i,j} = [\mathbf{P}_f]_{i,j} [\mathbf{C}]_{i,j} \quad (26)$$

where the correlation matrix coefficients are defined by $[\mathbf{C}]_{i,j} = \phi(|i - j|)$, for ϕ a smoothing function.

The smoothing function we use is a short-ranged predefined correlation function $\phi(r) = G(r/\rho_{\text{loc}})$, based on the Gaspari-Cohn function (Gaspari and Cohn 1999), for the localization radius ρ_{loc} ,

$$G(z) = \begin{cases} \text{if } 0 \leq r < 1: 1 - \frac{5}{3}z^2 + \frac{5}{8}z^3 + \frac{1}{2}z^4 - \frac{1}{4}z^5, \\ \text{if } 1 \leq r < 2: 4 - 5z + \frac{5}{3}z^2 + \frac{5}{8}z^3 - \frac{1}{2}z^4 + \frac{1}{12}z^5 - \frac{2}{3}z, \\ \text{if } r \geq 2: 0. \end{cases} \quad (27)$$

Based on the covariance localization, a new CME formulation can be derived. We call this formulation: the Global Localized CME (GL-CME). The GL-CME respects the original formulation Eq. (8), i.e., $f(\mathbf{y})$ is computed for the entire observation vector, while taking into account the regularized forecast error covariance matrix in the term Σ_k

$$\Sigma_k = \mathbf{H}_k [\mathbf{C} \circ \mathbf{P}_k^f] \mathbf{H}_k^T + \mathbf{R}. \quad (28)$$

In this case, the CME computation remains quite straightforward. However, concerning the computational cost, the regularization does not change the size of \mathbf{P}_k^f . The computational cost is as heavy as the original EnKF-formulation which adds to the cost of the application of a $M \times M$ Schur product, making this formulation not directly tractable in high dimensions. To do so, additional sophisticated techniques are required.

References

- Akaike H (1974). *A new look at the statistical model identification*. Autom. Contr., IEEE Transac. on 19: 716-723
- Asch, M., M. Bocquet and M. Nodet (2016). *Data assimilation: methods, algorithms, and applications*. Fundamentals of Algorithms. SIAM, Philadelphia.
- Balgovind, R., A. Dalcher, M. Ghil, and E. Kalnay (1983) *A stochastic-dynamic model for the spatial structure of forecast error statistics*. Mon. Wea. Rev., 111, 701722.
- Baum LE., T. Petrie, G. Soules and N. Weiss (1970). *A maximization technique occurring in the statistical analysis of probabilistic functions of Markov chains*. The Annals of Mathematical Statistics, 41:164-171.
- Bennett AF. (1992). *Inverse methods in physical oceanography*. Cambridge University Press, Cambridge, United Kingdom and New York, NY, USA.
- Bishop CH., BJ. Etherton and SJ. Majumdar (2001). *Adaptive sampling with the ensemble transform Kalman filter. Part I: Theoretical aspects*. Mon. Wea. Rev., 129: 420-436.
- Bocquet M. (2016). *Localization and the iterative ensemble Kalman smoother*. Q. J. R. Meteorol. Soc., 142: 1075-1089.
- Bocquet M. and A. Carrassi (2017). *Four-dimensional ensemble variational data assimilation and the unstable subspace*. Tellus A, 69: 1304504.
- Bourke, W. (1974). *A multilevel spectral model. I. Formulation and hemispheric integrations*. Mon. Wea. Rev., 102: 687-701.
- Bracco A., F. Kucharski, R. Kallumal and F. Molteni (2004). *Internal variability, external forcing and climate trends in multi-decadal AGCM ensembles*. Clim. Dyn., 23: 659-678
- Buehner M., PL. Houtekamer, C. Charette and HB. Mitchell (2010). *Intercomparison of variational data assimilation and the ensemble Kalman filter for global deterministic NWP. Part I: Description and single-observation experiments*. Mon. Wea. Rev., 138: 1550-1566.
- Burnham KP. and DR. Anderson (2002). *Model selection and inference: A practical information-theoretic approach*. Springer: New York, 2nd edition.
- Carrassi A. and S. Vannitsem (2016). *Deterministic treatment of model error in geophysical data assimilation*. In *Mathematical Paradigms of Climate Science*, Springer: 175-213.
- Carrassi A., M. Bocquet, A. Hannart and M. Ghil (2017). *Estimating model evidence using data assimilation*. Q. J. R. Meteorol. Soc., 143: 866-880.

- Carson J, M. Crucifix, S. Preston and RD. Wilkinson (2017). *Bayesian model selection for the glacial-interglacial cycle*. Journ. of the Roy. Stat. Soc.: Series C (Applied Statistics).
- Cressman, G.P. (1959) *An operational objective analysis system*. Mon. Wea. Rev., 87: 367-374.
- Daley R. (1991). *Atmospheric data analysis*. Cambridge University Press, Cambridge, United Kingdom.
- Dee DP. (1995). *On-line estimation of error covariance parameters for atmospheric data assimilation*. Mon. Wea. Rev., 123: 1128-1145.
- Donner, L. J., Seman, C. J., Hemler, R. S. and Fan, S. (2001). *A cumulus parameterization including mass fluxes, convective vertical velocities, and mesoscale effects: Thermodynamic and hydrological aspects in a general circulation model*. Journ. of clim., 14: 3444-3463.
- Elsheikh A, I. Hoteit and M. Wheeler (2014a). *Efficient bayesian inference of subsurface flow models using nested sampling and sparse polynomial chaos surrogates*. Comput. Methods Appl. Mech. Engrg., 269: 515-537.
- Elsheikh A, M. Wheeler and I. Hoteit (2014b). *Hybrid nested sampling algorithm for bayesian model selection applied to inverse subsurface flow problems*. J. Comput. Phys., 258: 319-337.
- Evensen G. (2009). *Data Assimilation: The Ensemble Kalman Filter*. Springer-Verlag/Berlin/Heidelberg, second edn.
- Gaspari G. and SE. Cohn (1999). *Construction of correlation functions in two and three dimensions*. Quart. J. Roy. Meteor. Soc., 125: 723-757.
- Ghil, M., M. Halem and R. Atlas (1979) *Time-continuous assimilation of remote-sounding data and its effect on weather forecasting*. Mon. Wea. Rev., 107: 140171.
- Ghil M. (1997). *Advances in sequential estimation for atmospheric and oceanic flows*. J. Meteor. Soc. Japan, 75: 289
- Ghil M. and P. Malanotte-Rizzoli (1991). *Data assimilation in meteorology and oceanography*. Adv. Geophys., 33: 141-266.
- Gini C. (1921). *Measurement of inequality of incomes*. Econ. J., 31: 124-126.
- Greybush SJ., E. Kalnay, T. Miyoshi, K. Ide, and BR. Hunt (2011). *Balance and ensemble Kalman filter localization techniques*. Mon. Wea. Rev., 139: 511-522.
- Haarsma RJ., EJD. Campos and F. Molteni (2003). *Atmospheric response to South Atlantic SST dipole*. Geophys. Res. Lett., 30
- Hamill, TM., JS. Whitaker and C. Snyder (2001). *Distance-dependent filtering of background error covariance estimates in an ensemble Kalman filter*. Mon. Wea. Rev., 129: 2776-2790.
- Harlim J. (2017). *Model error in data assimilation*. In *Nonlinear and Stochastic Climate Dynamics*, Franzke CLE. and TJ. O'Kane (eds.) Cambridge University Press: Cambridge, UK.
- Hannart A., J. Pearl, F.E.L. Otto, P. Naveau and M. Ghil (2016a). *Causal counterfactual theory for the attribution of weather and climate-related events*. Bull. Am. Meteorol. Soc., 97: 99-110.
- Hannart A., A. Carrassi, M. Bocquet, M. Ghil, P. Naveau, M. Pulido, J. Ruiz and P. Tandeo (2016b). *DADA: data assimilation for the detection and attribution of weather and climate-related events*. Climatic Change, 136: 155-174.
- Houtekamer PL. and HL. Mitchell (2001). *A sequential ensemble Kalman filter for atmospheric data assimilation*. Mon. Wea. Rev., 129: 123-137.
- Hunt B., EJ. Kostelich and I. Szunyogh (2007). *Efficient data assimilation for spatiotemporal chaos: A local ensemble transform Kalman filter*. Physica D, 230: 112-126.
- Ide, K., P. Courtier, M. Ghil, and A. Lorenc (1997). *Unified notation for data assimilation: Operational, sequential and variational*. J. Meteor. Soc. Japan, 75: 181-189.
- Kalnay, E. (2003). *Atmospheric modeling, data assimilation and predictability*. Cambridge university press.
- Kucharski F. and F. Molteni (2003). *On non-linearities in a forced North Atlantic Oscillation*. Clim. Dyn., 21: 677-687
- Kucharski F., F. Molteni and A. Bracco (2006). *Decadal interactions between the western tropical Pacific and the North Atlantic Oscillation*. Clim. Dyn., 26: 79-91
- Lermusiaux PFJ. (2006). *Uncertainty estimation and prediction for interdisciplinary ocean dynamics*. J. Comp. Phys., 217: 176-199.
- Lorenz, E. N. (1996). *Predictability: a problem partly solved*. Seminar on Predictability, 4–8 September 1995, European Centre for Medium-range Weather Forecasting, Shinfield Park, UK, pp. 1–18.
- Lorenz, EN. and KA. Emanuel (1998). *Optimal sites for supplementary weather observations: simulation with a small model*. J. Atmos. Sci., 55: 399-414.
- Metz CE. (1978). *Basic principles of ROC analysis*. Semin. Nucl. Med., 8: 283-298.
- Molteni F. (2003). *Atmospheric simulations using a GCM with simplified physical parameterizations. I: model climatology and variability in multi-decadal experiments*. Clim. Dyn., 20: 175-191.
- Miyoshi T. (2005). *Ensemble Kalman filter experiments with a primitive-equation global model*. Ph.D. dissertation, University of Maryland, 197 pp.
- Miyoshi T. and S. Yamane (2007). *Local ensemble transform Kalman filtering with an AGCM at a T159/L48 resolution*. Mon. Wea. Rev., 135: 3841-3861.
- Miyoshi T., S. Yamane and T. Enomoto (2007). *Localizing the error covariance by physical distances within a Local Ensemble Transform Kalman Filter (LETKF)*. SOLA, 3: 89-92
- Neelin, J. David and Bracco, Annalisa and Luo, Hao and McWilliams, James C. and Meyerson, Joyce E. *Considerations for parameter optimization and sensitivity in climate models*. Proc. Natl. Acad. Sci. USA, 107:21349-21354.
- Otsuka S. and T. Miyoshi (2015). *A Bayesian optimization approach to multimodel ensemble Kalman filter with a low-order model*. Mon. Wea. Rev., 143: 2001-2012.
- Ott, E., BR. Hunt, I. Szunyogh, M. Corazza, E. Kalnay, DJ. Patil, A. Yorke, AV. Zimin and EJ. Kostelich (2002). *Exploiting local low dimensionality of the atmospheric dynamics for efficient ensemble Kalman filtering*.

- Ott, E., BR. Hunt, I. Szunyogh, AV. Zimin, EJ. Kostelich, M. Corazza, E. Kalnay, DJ. Patil and A. Yorke (2004). *A local ensemble Kalman filter for atmospheric data assimilation*. Tellus A, 56: 415-428.
- Raanes PN, A. Carrassi and L. Bertino (2015). *Extending the square root method to account for additive forecast noise in ensemble methods*. Mon. Wea. Rev., 143: 3857-3873.
- Reich S and C. Cotter (2015). *Probabilistic Forecasting and Bayesian Data Assimilation*. Cambridge University Press, Cambridge, United Kingdom.
- Saha S., M. Shrinivas, HL. Pan, X. Wu, J. Wang, S. Nadiga, P. Tripp, R. Kistler, J. Woollen, D. Behringer and others (2010). *The NCEP Climate Forecast System Reanalysis*. Bull. Amer. Meteor. Soc., 91: 1010-1057.
- Saha S., M. Shrinivas, X. Wu, J. Wang, S. Nadiga, P. Tripp, D. Behringer, YT. Hou, HY. Chuang, M. Iredell and others (2014). *The NCEP Climate Forecast System version 2*. J. Climate, 27: 2185-2208.
- Sakov P. and L. Bertino (2011). *Relation between two common localisation methods for the EnKF*. Comput. Geosci., 15: 225-237.
- Sakov P., F. Counillon, L. Bertino, KA. Lisaeter, PR. Oke and A. Korablev (2012). *Topaz4 : an ocean-sea ice data assimilation system for the north atlantic and arctic*. Ocean Sci., 8: 633-656.
- Schwarz G. (1978). *Estimating the dimension of a model*. Ann. of Stat., 6: 461-464.
- Tiedke M. (1993). *A comprehensive mass flux scheme for cumulus parametrization in large-scale models*. Mon. Wea. Rev., 117: 1779-1800.
- Whitaker JS., TM. Hamill, X. Wei, Y. Song and Z. Toth (2008). *Ensemble data assimilation with the NCEP global forecast system*. Mon. Wea. Rev., 136: 463-482.
- Winiarek V., J. Vira, M. Bocquet, M. Sofiev and O. Saunier (2011). *Towards the operational estimation of a radiological plume using data assimilation after a radiological accidental atmospheric release*. Atmos. Environ. 45: 2944-2955.